5-1-2004

Dynamics of Pectoral Fin Rowing in a Fish with an Extreme Rowing Stroke: The threespine stickleback (Gasterosteus aculeatus)

Jeffrey A. Walker Ph.D.
University of Southern Maine, walker@usm.maine.edu

Recommended Citation
Walker, J. A. (2004). Dynamics of pectoral fin rowing in a fish with an extreme rowing stroke: the threespine stickleback (Gasterosteus aculeatus). Journal Of Experimental Biology, 207(11), 1925-1939.

The Journal of Experimental Biology 207, 1925-1939
Published by The Company of Biologists 2004
doi:10.1242/jeb.00994

Dynamics of pectoral fin rowing in a fish with an extreme rowing stroke: the threespine stickleback (*Gasterosteus aculeatus*)

Jeffrey A. Walker

Department of Biological Sciences, University of Southern Maine, 96 Falmouth Street, Portland, ME 04103, USA

e-mail: walker@usm.maine.edu

Accepted 22 March 2004

Summary

The dynamics of pectoral fin rowing in the threespine stickleback are investigated by measuring the instantaneous force balance on freely swimming fish throughout the stroke cycle and comparing the measured forces with fin motions and an unsteady, blade-element model of pectoral fin propulsion. Both measured and modeled forces suggest that attached vortex and circulatory forces and not inertial (added mass) forces dominate the force balance. Peak forces occur at midstrokes. There is no evidence for large force peaks at the stroke transitions due to either rapid fin rotation (supination) or rapid fin closure against the body. The energetics of pectoral fin rowing are estimated using the unsteady blade-element model and an indirect method based on the center of mass dynamics. The results indicate that the mechanical efficiency of pectoral fin rowing is low (0.1–0.3) relative to a flapping mechanism and possibly relative to axial undulation at comparable speeds.

Key words: locomotion, unsteady fluid dynamics, energetics, blade-element analysis, circulatory force, acceleration reaction, mechanical power, mechanical efficiency.

Introduction

Pectoral fin motions for propulsion and maneuvering are highly variable among fishes, but at least some of this variation can be summarized by an axis in which fore–aft rowing characterizes one extreme while dorso-ventral flapping characterizes the opposite extreme (Breder, 1926; Lindsey, 1978; Webb and Blake, 1985; Walker and Westneat, 2002a,b). The geometry of pectoral fin motion has important dynamic consequences (the magnitude of lift and thrust generated throughout the stroke cycle and how much energy is wasted in the generation of thrust) that should affect how a fish exploits resources in its environment (Walker and Westneat, 2000). In order to explore the performance consequences of pectoral fin motion in more detail, we need good comparative measures of how different pectoral fin designs generate propulsive forces.

There have been many previous attempts to infer the dynamics of pectoral fin propulsion in free-swimming fishes from an analysis of either the pectoral fin kinematics (Webb, 1973; Blake, 1979, 1980; Geerlink, 1983; Archer and Johnston, 1989; Gibb et al., 1994; Arreolla and Westneat, 1996; Gordon et al., 1996; Lauder and Jayne, 1996; Drucker and Jensen, 1997; Walker and Westneat, 1997, 2002a; Hove et al., 2001; Ramamurti et al., 2002) or the pectoral fin's wake geometry (Drucker and Lauder, 1999, 2000, 2001, 2003). Investigations of pectoral fin energetics are few and have relied on either oxygen consumption measures (Webb, 1974; Gordon et al., 1989; Korsmeyer et al., 2002) or quasi-steady blade-element models of real (Blake, 1979, 1980) or theoretical fish (Walker and Westneat, 2000).

Blake's model of the dynamics and energetics of pectoral fin rowing (Blake, 1979, 1980) has been influential in the aquatic locomotion literature. The major conclusions of the model are that (1) while the acceleration reaction contributes to the work budget, its positive and negative contributions to the mean thrust cancel and (2) the overall mechanical efficiency, η, of the fin is low relative to the efficiency of body-and-caudal (BCF) swimming at preferred swimming speeds but is, perhaps, higher than that of BCF swimming at slow swimming speeds (no estimate of η for BCF swimming at slow speeds was given so this last assertion cannot be evaluated). Unfortunately, there was no attempt to verify the predictions of the model with empirical data and, consequently, the validity of the results remains in question.

The dynamics of pectoral fin propulsion have been inferred indirectly by analysis of the center of mass kinematics. A qualitative analysis of body displacement relative to stroke cycle position in the flapping stroke of the shiner surfperch, *Cymatogaster aggregata*, indicated that thrust is characteristic of both down- and upstrokes and that positive and negative lift alternate between strokes (Webb, 1973). The mean acceleration over each halfstroke was used to estimate the net downstroke thrust and upstroke thrust in the queen coris, *Coris frerei* (Geerlink, 1983). A net negative thrust was found for the downstroke and a net positive thrust was found for the upstroke. The instantaneous accelerations of the body in the bird wrasse, *Gomphosus varius*, were used to infer the downstroke and upstroke forces (Walker and Westneat, 1997).

At all speeds, thrust was predominantly generated during the upstroke but some thrust (between 12% and 22%) was generated during the downstroke. By contrast, positive lift was generated during the downstroke at all speeds but only at slow speeds during the upstroke.

Recently, digital particle image velocimetry (DPIV) has been used to measure the net force over each halfstroke in the bluegill, *Lepomis macrochirus*, and the black surfperch, *Embiotoca jacksoni* (Drucker and Lauder, 1999, 2000). In contrast to previously described results for other fishes, the sunfish at low speeds and black surfperch at moderate to high speeds generated most of the thrust during the downstroke. Similar to previous results, lift in both species was positive during the downstroke and negative (or absent) during the upstroke.

These alternative methods for inferring the dynamics of pectoral fin propulsion (body displacement and DPIV) have only been applied to fishes that present more of flapping stroke than rowing stroke (with the exception, perhaps, of *L. macrochirus*, whose stroke is difficult to place along a rowing–flapping axis). Similarly, all work on the energetics of pectoral fin propulsion using oxygen consumption methods has been applied only to fishes that present more of a flapping stroke (Webb, 1974; Gordon et al., 1989; Korsmeyer et al., 2002). Consequently, our only data on the dynamics and energetics of the rowing stroke of fishes are from a blade-element model whose results were not verified with any empirically measured data, such as center of mass displacement, oxygen consumption or wake geometry. The dynamics of pectoral fin rowing were recently investigated with a non-flexing, motor-driven fin resembling the planform of the pectoral fin of the centrarchid fish, *Micropterus salmoides* (Kato, 1999). Application of these results to the fins of teleost fishes is limited, since teleost fins are highly flexible and deform as a consequence of both elastic and fluid dynamic stresses (Geerlink, 1983; Archer and Johnston, 1989; Gibb et al., 1994; Lauder and Jayne, 1996; Westneat, 1996; Drucker and Jensen, 1997; Westneat and Walker, 1997).

To rectify this major gap in our understanding of pectoral fin function in fishes, the dynamics and energetics of a pectoral fin rower, the threespine stickleback, *Gasterosteus aculeatus*, are presented. This work has three goals. First, to measure empirically the instantaneous lift and thrust balance on the body throughout a complete stroke cycle. Second, to apply a hydrodynamic model to measured fin kinematics in order to estimate the various contributions and timings of circulatory and added mass forces on net lift and thrust. The validity of the model is checked by comparing the modeled and measured estimates of lift and thrust. Third, to estimate the economic effectiveness of the rowing stroke by estimating its mechanical efficiency, which is the ratio of the useful to the total work done by the fin on the water.

Indirect measures of instantaneous thrust and lift generated by the fins are estimated from a force-balance model using the digitized displacement of the center of mass (Walker and Westneat, 1997, 2002a). This indirect measurement relies on few assumptions (see Materials and methods) and allows the measurement of lift and thrust in freely swimming fish. An indirect measure of lift and thrust could be estimated more accurately by tethering an individual to a force transducer, an experimental technique that is common in insects but has never been applied to fishes. Many of the assumptions (e.g. pectoral fin dynamics alone balance weight and drag) of the indirect force measurement method used in this study also apply to direct force measurements from tethered individuals. Similarly, the decomposition of the net lift and thrust into circulatory and added mass components requires a (virtual or physical) model. The major limitations to tethering experiments are (1) simulating a specific speed and (2) inducing the animal to activate the same kinematic patterns at this simulated speed as it would if moving freely at this speed. Direct measurements of circulatory forces on a fin would involve either instrumenting the fin with a series of pressure transducers or measuring the distribution of fluid velocities around the fin using quantitative flow visualization, such as DPIV. Neither method is technologically mature enough to apply to the small, highly deformable fins of the stickleback. DPIV is, with few exceptions (Anderson et al., 2001), restricted to the wake behind a fin and can, consequently, only give a summary (such as the mean lift and thrust over a stroke) of the fluid dynamics of the fin stroke. While qualitative flow imaging (Srygley and Thomas, 2002) has been successful in identifying key fluid dynamic features at a fluid–wing boundary (such as leading edge vortices), one cannot estimate instantaneous forces with this technique. One possible solution that might allow the estimate of the instantaneous force balance on a flexible, pectoral fin is the recently developed defocusing DPIV system used to measure the velocity distribution throughout a volume of fluid surrounding a deforming object (Pereira and Gharib, 2002).

To estimate the contribution of circulatory and added mass forces and to explore the timings of these components, a previously developed, unsteady blade-element model (Walker and Westneat, 2000; Walker, 2002b) is further generalized to allow its application to the stickleback kinematics. The chief advantage of the model is its trivial computational burden, allowing its rapid application to a diverse array of fin movements. Despite its computational simplicity, the model has been remarkably effective at recovering most of the dynamic patterns identified by either robotic models or by more sophisticated virtual models. While motor-driven robotic fins offer an elegant method for investigating lift and thrust generation on an oscillating plate, current robotic models are not adequate for modeling stickleback fins because the actuation mechanism necessary for the types of fin motions presented by a stickleback pectoral fin (active control of multiple joints) is far more complex than the mechanisms found in current robotic fins and wings (active control of a single joint).

A model for indirectly measuring mechanical power and efficiency from measured body accelerations and wing kinematics (Pennycuick et al., 2000) is generalized and applied

to the stickleback data. These measured estimates of power and efficiency are compared to modeled estimates of power and efficiency computed from the blade-element model. Using a model of oxycalorific equivalents and swimming muscle efficiency, one can convert measures of O_2 consumption to estimates of the mean mechanical power over a stroke cycle or compute an estimate of mechanical efficiency. Ward et al. (2001) and Schultz and Webb (2002) have critically reviewed some of the assumptions with this type of modeling. Even if we had good estimates of muscle efficiency for stickleback, respirometry for individual fish the size of sticklebacks swimming at uniform speeds is not a viable option because of constraints on the design of water tunnel respirometers (J. Herskin and J. F. Steffenson, personal communication). One advantage of the indirect measure and modeled measure of mechanical power and efficiency is the ability to apply these methods to smaller fish.

Materials and methods

Sticklebacks (*Gasterosteus aculeatus* Linnaeus 1758) are small fish that inhabit coastal marine and freshwater throughout much of the temperate northern hemisphere (Bell and Foster, 1994). The sticklebacks in this study are anadromous individuals that were captured in Rabbit Slough, near Wasilla, AK, USA. Fish were filmed swimming in freshwater in a flow tank designed after Vogel and LaBarbera (1978). A centimeter grid was placed on the rear side of the tank to calibrate video images. Water temperature in the flow tank was maintained at 21±1°C. Fin stroke sequences were filmed in lateral view at 250 Hz using a RedLake Motionscope high-speed digital camera. Digital sequences were saved as QuickTime® files and digitized using a modification of the public domain NIH Image program (developed at the US National Institutes of Health and available on the Internet at http://rsb.info.nih.gov/nih-image/) for the Apple Macintosh (the modification, which is available from the author upon request). Eighteen sequences from six individuals swimming at one of three speeds were archived for further analysis. Following filming, fish were sacrificed in MS-222, measured and weighed (Table 1). Fin aspect ratio and standardized first through third moments of fin area (Ellington, 1984a) were measured on the preserved specimens.

Kinematics

Stroke frequency (*n*), averaged over multiple (5–10) beats, stroke angle (Φ) and stroke plane angle (β) were estimated from all 18 sequences (methods following Walker and Westneat, 1997).

Instantaneous fin geometry was measured for six sequences. In order to justify the methods for measuring this geometry it is necessary to describe the stickleback fin stroke qualitatively. The largely fore–aft stroke is described and illustrated from a left lateral view (Fig. 1). QuickTime® videos of selected sequences are available at http://www.usm.maine.edu/~walker/movies.html.

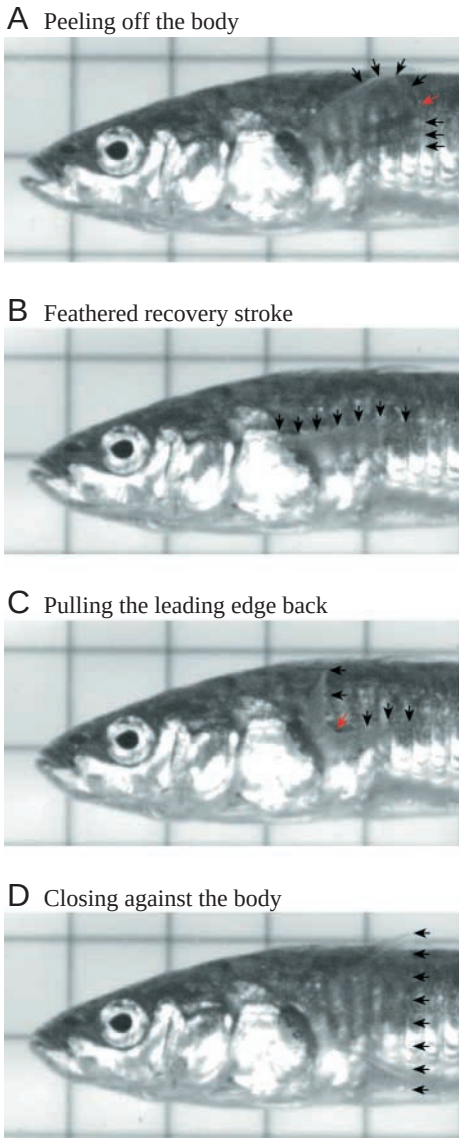

Fig. 1. These stills from a rowing stroke of the stickleback highlight (A) how the sharp bend in the fin allows it to achieve a feathered orientation as it is pulled off the body at the initiation of the recovery stroke, (B) the feathered fin during the recovery stroke, (C) how the sharp bend in the fin allows the fish to achieve a broadside orientation by pulling the leading edge at the start of the power stroke (rather than rigidly rotating the appendage as in a fruitfly) and (D) the broadside orientation during the power stroke and close against the body. The black arrows mark the distal edge of the fin while the red arrows mark the location along the distal edge of the sharp bend.

Immediately prior to the recovery stroke, the fin rotates counterclockwise along the body. The first part of the recovery stroke is characterized by the fin rays peeling off the body starting with the leading edge ray and proceeding, ray by ray, to the trailing edge ray. As the leading edge rays peel off the body, the trailing rays continue to rotate counterclockwise along the body. The point marked by the red arrow in Fig. 1A illustrates the break point along the distal edge separating the

hydrodynamically active leading edge region from the inactive trailing region. The trailing edge ray peels off the body at about the time it reaches the same dorso-ventral position as the leading edge ray. The second part of the recovery stroke is characterized by the fin translating anteriorly with the plane of the fan pitched slightly ventrally (Fig. 1B). About the time the leading edge ray reaches its most forward position, the fin rays distinctly spread out, forming a larger surface area.

The power stroke begins with a rapid posterodorsal translation of the leading edge ray. The dorsal translation of the leading edge causes a clockwise rotation of the anterior fin surface into a broadside orientation (Fig. 1C). A wave of fin ray rotation passes posteriorly as the leading edge rays translate posteriorly. During the posterior translation of the leading edge surface, the trailing rays stop translating anteriorly but may move slightly ventrally. The red arrow in Fig. 1C illustrates the break point on the distal edge separating the leading edge region, which is rapidly translating posteriorly, from the trailing edge region, which has largely stopped translating. During this time, the fin is sharply curved at this break point. It is important to note that the fin does not rigidly rotate into a broadside orientation but instead resembles the peeling of a carpet off a floor by pulling one end back and up. Following rotation, all fin rays simultaneously translated back toward the body (Fig. 1D). The backstroke ended when the largely posteriorly directed fin rays closed against the body.

To digitize the fin geometry throughout fin motion, the positions of the dorsal fin base, ventral fin base, leading edge tip and trailing edge tip were digitized in each frame. An additional landmark was digitized to mark the break point along the distal edge separating the active from inactive regions of the fin during the first part of the recovery and power strokes. Only the active part of the fin is modeled. During the second part of each stroke, the entire fin is effectively active.

A blade-element (or strip) method was used to infer the geometry of the fin from base to distal edge. The implemented model assumes that the orientation of the fin base does not itself rotate during the stroke, that the pitch of the fin varies linearly from the fin base to the distal edge (that is, it twists down its span), that the span of the fin is constant (that is, the bony rays do not bend due to fluid dynamic loading) and that there is no camber along a chord. The first three of these assumptions are easily relaxed but would require more detailed kinematic measures to account for the variation. While the assumption of a constant fin base angle is met for the stickleback because of the relative immobility of the joints within its shoulder plate, this assumption (which, again, can be relaxed if the appropriate kinematics are measured) is certainly violated in some fishes (Drucker and Lauder, 2003). The last assumption (zero camber) could be relaxed only with the appropriate empirical force coefficients.

The fin stroke cycle begins with fin abduction and ends when the fin closes against the body (any pause phase with the fin against the body is not modeled). The stroke cycle has a period (τ) that was divided into N=250/τ frames each of time $\Delta\tau$=1/250 s. Time was standardized not across the entire cycle but within each stroke. Following this standardization, the total time for each stroke is 0.5 and the standardized period ($\hat{\tau}$) is 1. Finally, the fin, with span R, was arbitrarily divided along its span into 11 elements with equal width, Δr=R/11. The length-specific radial position is $\hat{r}$=r/R, where r is distance from the fin base. In the following, the bracketed subscripts indicate that a variable is a function of time (t) and/or radial position along the span (r).

The position of the fin, $\gamma_{(t)}$, was estimated as the angle between the leading edge ray, projected onto the stroke plane, and a unit vector directed back along the x-axis. In this coordinate system, $\gamma_{(t)}$ is 0° when the leading edge is back against the body and 90° when perpendicular to the body axis. The fin articulates at its base with an angle, θ_b, relative to the horizontal and oscillates about a flapping axis with an angle, θ_f, relative to the horizontal (θ_f is normal to the stroke plane). While often modeled as the same angle, θ_b and θ_f differ in the stickleback. The difference between the angles, θ_b–θ_f, is δ. As the fin translates, it twists down its span. The pitch, $\alpha_{(r,t)}$, of the distal edge of the fin was estimated as the angle between the distal edge chord and the fin base chord following the projection of both chords into the sagittal plane. The distal edge chord was measured for the active part of the fin only (from the leading edge to the break point) and α_R, therefore, reflects the pitch of the functional portion of the fin. The pitch, $\alpha_{(r,t)}$, at the radial position $\hat{r}$ along the span is $\hat{r}\alpha_{(r,t)}$ while the geometric angle of attack (angle relative to free stream), $\alpha_{g(r,t)}$, is:

$$\alpha_{g(r,t)} = \theta_b - \delta\cos\gamma_{(t)} + \alpha_{(r,t)} . \quad (1)$$

Because the data were digitized from a two-dimensional lateral view (the xz plane), the coordinates of the third (y) dimension had to be reconstructed using the known lengths of the fin rays. This method assumes that spanwise deformations of the fin rays are small relative to their length. Because the reconstruction error is confined to the y-axis, estimates of $\alpha_{(r,t)}$ and $\gamma_{(t)}$ will be largely confined to that part of the stroke when the fin is near its maximally adducted position (back against the body). The accuracy of this pseudo-3-D method has previously been tested using a data set in which the 3-D coordinates were measured. The median absolute difference in the estimate of the stroke angle between the measured-3-D and pseudo-3-D coordinates was 3.5° (Walker and Westneat, 2002b).

Net force balance

In a fish swimming at a steady speed, lift and thrust must balance weight and drag. I assume that the lift and thrust generated by control surfaces other than the pectoral fins are trivial relative to that generated by the oscillating pectoral fins, and, therefore, the instantaneous thrust and lift acting on the body is effectively equal to that generated by the fins (this assumption is discussed further in the Discussion). The instantaneous force on the body of a freely swimming fish cannot be directly measured, but its fore–aft (F_x) and up–down (F_z) components can be estimated by simply multiplying either the fore–aft or up–down acceleration component by the mass of the accelerating system. I refer to this estimate of the

instantaneous force as the measured force (as opposed to the modeled force, which is estimated from the unsteady, blade-element model – see below). From the measured force components, measured lift and thrust were estimated by:

$$L_{\text{measured(t)}} = (M_F + M_{Az})(dU_z/dt) + W\,, \quad (2)$$

$$T_{\text{measured(t)}} = (M_F + M_{Ax})(dU_x/dt) + D\,, \quad (3)$$

where M_F is mass of the fish, M_{Ax} and M_{Az} are the added masses in the direction of thrust (x-axis) or lift (z-axis), dU/dt is the acceleration of the body in the direction of thrust or lift, D is the dead-drag on the body, and W is the weight of the fish in water. The added mass of the body associated with fore–aft or up–down acceleration was not directly measured but estimated using empirically derived coefficients measured for bodies of revolution with similar dimensions (Brennen, 1982):

$$M_A = \tfrac{4}{3}\pi\rho\mu(l d_{max} b_{max})/2\,, \quad (4)$$

where ρ is the density of freshwater at 20°C, l is standard length, d_{max} is maximum body depth, b_{max} is maximum body breadth, and the added mass coefficients (μ) in the fore–aft (x) or up–down (z) direction are 0.405 and 0.9255, respectively (Brennen, 1982). The added mass of the median and caudal fins, which would contribute little in the x and z directions, was not included in this model. D was estimated for a body of revolution using (Hoerner, 1965):

$$D = \tfrac{1}{2}\rho A_{wet} U^2 C_D\,, \quad (5)$$

where U is the free stream speed, A is the wetted area of the body according to:

$$A_{wet} = 0.7l \times 2\pi \sqrt{\frac{d_{max}^2 + b_{max}^2}{8}}\,, \quad (6)$$

C_D is the dead-drag coefficient of the body:

$$C_D = \frac{1.328}{\sqrt{Re}}\,(1 + f^{-\frac{3}{2}} + 0.11 f^{-2})\,, \quad (7)$$

and f is the fineness ratio, $l(d_{max}b_{max})^{-\frac{1}{2}}$.

Body acceleration was estimated by using numerical differentiation. To measure displacement of the body, a landmark near the approximate center of mass was located and digitized frame-by-frame. Center of mass displacement in 18 sequences from six individuals was digitized. Each sequence consisted of two stroke cycles and began and ended with the fin maximally abducted (end of the recovery stroke). While the entire two-cycle sequence was digitized and fit with a spline function (see below), only the central fin beat, beginning with fin abduction and ending with the fin closing against the body, was compared among sequences. In order to determine the error in the estimate of body displacement, three arbitrarily chosen sequences were each digitized three times. The grand mean deviation (averaged over all points and sequences) was 0.0039 cm (0.00054 *SL*) for the x (anteroposterior) axis and 0.0047 cm (0.00065 *SL*) for the z (dorsoventral) axis.

The displacement data were smoothed and twice differentiated using a quintic spline function. The optimal smoothing parameter for the spline was estimated using the true predicted mean-squared error (MD=3) criterion (Woltring, 1985, 1986). In a large simulation study, the MSE quintic spline algorithm performed well compared with other published numerical differentiation algorithms (Walker, 1998) and is available in the software QuickSAND (available from the author upon request). The mean standard deviation for the three sequences digitized three times each was 0.363 pixels on the x-axis and 0.41 pixels on the y-axis. In addition to digitizing error, measurement error includes the component due to the transformation to a discrete (pixel) space. This component has a maximum error of 0.5 pixels; a reasonable assumption of its average is 0.25 pixels. The total variance, which is the sum of the squares of these two components, was used as the predicted MSE.

Unsteady model of fin dynamics and energetics

The dynamics of unsteady, oscillating foils can be modeled with reasonable accuracy using a simple, unsteady blade-element model (Walker and Westneat, 2000; Sane and Dickinson, 2002; Walker, 2002b). A blade-element model allowing for both unsteady circulatory and added mass forces for a limb oscillating about its root was developed previously (Walker and Westneat, 2000). Accuracy of the model (tested by comparison with robotic oscillating plates) is discussed in the original paper and, more thoroughly, in Walker (2002b). The kinematics of the model are similar to that of Fung (1993), but allowed the flapping axis to be arbitrary (not necessarily 0°), and to that of DeLaurier (1993), but allowed for large amplitude motions. Because $\theta_f \neq \theta_b$ in the stickleback, the model is further generalized here.

The normal, $v_{n(r,t)}$, and chordwise, $v_{x(r,t)}$, flow due to fin translation and rotation are:

$$v_{n(r,t)} = \dot{h}_{(r,t)} \cos[\alpha_{(r,t)} + \delta \sin\gamma_{(t)}] + U_{n(t)} \sin[\alpha_{g(r,t)}] + [\hat{x}_o - \hat{x}_{r(r)}] c_{(r,t)} \dot{\alpha}_{(r,t)}\,, \quad (8)$$

$$v_{x(r,t)} = -\dot{h}_{(r,t)} \sin[\alpha_{(r,t)} + \delta \sin\gamma_{(t)}] + U_{n(t)} \cos[\alpha_{g(r,t)}]\,. \quad (9)$$

The first component of equations 8 and 9 is due to the fin element translating with a speed, $\dot{h}_{(r,t)} = \hat{r} R \dot{\gamma}_{(t)}$, due to fin oscillation. The second component is due to the fish translating through the water at speed U, where the component of U normal to the leading edge is:

$$U_{n(t)} = U[1 - |\cos\gamma_{(t)}| \sin\theta_f]\,. \quad (10)$$

The third component (in equation 8) is due to the fin rotating around a spanwise axis located $\hat{x}_{r(r)} c_{(r,t)}$ from the leading edge and a chordwise center of incident flow located $\hat{x}_o c_{(r,t)}$ from the leading edge, where $\hat{x}_o$ or $\hat{x}_{r(r)}$ is a percent distance along the chord and $c_{(r,t)}$ is chord length. The first component of equations 8, 9 gives rise to the translational circulatory force, and the third component gives rise to the rotational circulatory force (Ellington, 1984b; Dickinson et al., 1999); the second component is absent from the hovering situations considered by Ellington and Dickinson.

The (hydrodynamic) angle of attack, or angle of incidence,

$\alpha'_{(r,t)}$, is $\pm\tan^{-1}(v_{n(r,t)}/v_{x(r,t)})$ where the $\pm$ takes the sign of $v_{x(r,t)}$. This angle is used to estimate the lift and drag coefficients (see below) and the components of the combined translational and rotational forces normal to and parallel with the fin chord:

$$dF_{n(r,t)} = dL'_{(r,t)}\cos\alpha'_{(r,t)} + dD'_{(r,t)}\sin\alpha'_{(r,t)}\,, \quad (11)$$

$$dF_{x(r,t)} = dL'_{(r,t)}\sin\alpha'_{(r,t)} + dD'_{(r,t)}\cos\alpha'_{(r,t)}\,. \quad (12)$$

($dF_{n(r,t)}$ is positive out from the medial surface of the fin, while $dF_{x(r,t)}$ is positive toward the leading edge.) $dL'_{(r,t)}$ and $dD'_{(r,t)}$, the components of the translational and rotational circulatory forces normal to and parallel with the local stream, are:

$$dL'_{(r,t)} = \tfrac{1}{2}\rho v^2_{(r,t)} c_{(r,t)} C'_{L(r,t)}\Delta r\,, \quad (13)$$

$$dD'_{(r,t)} = \tfrac{1}{2}\rho v^2_{(r,t)} c_{(r,t)} C'_{D(r,t)}\Delta r\,, \quad (14)$$

where

$$v^2_{(r,t)} = v^2_{n(r,t)} + v^2_{x(r,t)}\,, \quad (15)$$

Δr is the width of the chord element, and $C'_{L(r,t)}$ and $C'_{D(r,t)}$ are the lift and drag coefficients (see below). The combined translational and rotational circulatory lift and thrust on a blade element are:

$$dL_{c(r,t)} = \{dF_{n(r,t)}\cos[\alpha_{g(r,t)}] + dF_{x(r,t)}\sin[\alpha_{g(r,t)}]\} [\sin\gamma_{(t)}\cos^2\theta_f + \sin^2\theta_f]\,, \quad (16)$$

$$dT_{c(r,t)} = \{-dF_{n(r,t)}\sin[\alpha_{g(r,t)}] + dF_{x(r,t)}\cos[\alpha_{g(r,t)}]\} [\sin\gamma_{(t)}\sin^2\theta_f + \cos^2\theta_f]\,. \quad (17)$$

The added mass force normal to the fin element is:

$$dF_{a(r,t)} = \frac{\pi}{4}\rho c^2_{(r,t)}\dot{v}_{n(r,t)}\mu_n\Delta r\,, \quad (18)$$

where μ_n is the added mass coefficient of the fin section (a value of 1.0 was used). The section lift and thrust components of $dF_{a(r,t)}$ are:

$$dL_{a(r,t)} = dF_{a(r,t)}\cos[\alpha_{g(r,t)}][\sin\gamma_{(t)}\cos^2\theta_f + \sin^2\theta_f]\,, \quad (19)$$

$$dT_{a(r,t)} = -dF_{a(r,t)}\sin[\alpha_{g(r,t)}][\sin\gamma_{(t)}\sin^2\theta_f + \cos^2\theta_f]\,. \quad (20)$$

The sectional power needed to oscillate the fins against the water is:

$$dP_{c(r,t)} = dF_{n(r,t)}\{\dot{h}_{(r,t)}\cos[\alpha_{(r,t)} + \delta\sin\gamma_{(t)}] + [\dot{\hat{x}}_p - \dot{\hat{x}}_{r(r)}]c_{(r,t)}\dot{\alpha}_{(r,t)}\} + dF_{x(r,t)}\dot{h}_{(r,t)}\sin[\alpha_{(r,t)} + \delta]\,, \quad (21)$$

and the power need to accelerate the water is:

$$dP_{a(r,t)} = dF_{a(r,t)}\{\dot{h}_{(r,t)}\cos[\alpha_{(r,t)} + \delta\sin\gamma_{(t)}] + [\dot{\hat{x}}_p - \dot{\hat{x}}_{r(r)}]c_{(r,t)}\dot{\alpha}_{(r,t)}\}\,. \quad (22)$$

Sectional lift, thrust and power are summed along the span and multiplied by two to give the total modeled lift [$L_{modeled(t)}$], thrust [$T_{modeled(t)}$] and power [$P_{modeled(t)}$] for the pair of fins. Note that while the total modeled force includes a lateral component, this component is not reported because there is no measured lateral component for comparison. The mechanical efficiency, η, is a measure of the percentage of total work done by the fin on the water that is useful (that is, contributes to thrust; another way to think of this is the percentage of the total work that is not wasted). The quasi-steady estimate of the mechanical efficiency is:

$$\eta_{modeled} = \frac{\bar{T}_{modeled}U}{\bar{P}_{modeled}}\,. \quad (23)$$

Coefficient model

In a previous blade-element model, lift and drag coefficients derived from a robotic wing oscillating at a Reynold's number (*Re*) of 192 (Dickinson et al., 1999) were used to model the dynamics of rowing and flapping propulsion because these were the only ones available that accounted for the augmented effect of an attached leading edge or trailing edge vortex (Walker and Westneat, 2000). These unsteady coefficients additionally include the effects of an unmeasured induced velocity component. Scale (*Re*) has only a small effect on $C_{L(r,t)}$ and $C_{D(r,t)}$ in the range $10^2<Re<10^5$ (Usherwood and Ellington, 2002), which suggests that the robotic wing coefficients should give good estimates of force magnitudes for any oscillating airfoil in this range. Because of time delays in the generation of force production on impulsively started plates, $C_{L(r,t)}$ and $C_{D(r,t)}$ were reduced by the Wagner function (Fung, 1993):

$$C'_{F(r,t)} = \left(1 - \frac{2}{4 + \tau_{(r,t)}}\right) C_{F(r,t)}\,, \quad (24)$$

where $\tau_{(r,t)}$ is the number of chord lengths traveled following stroke reversal.

A measured force model of power and efficiency

The quasi-steady model of pectoral fin energetics requires accurate estimates of detailed fin kinematics and assumes that circulatory and added mass forces dominate the force balance and that these forces can be accurately estimated with quasi-steady coefficients. Pennycuick et al. (2000) made the novel suggestion that measured forces (specifically $L_{measured}$) be used in place of the modeled forces to compute mean work and power. Their method assumed a vertical stroke plane (θ_b and θ_f=0), a constant pitch of 0° down the span throughout the stroke, and a constant C_L down the span at any one time in the stroke cycle (Pennycuick et al., 2000). Note that the equal C_L assumption is only compatible with the two kinematic assumptions if the local stream vector is dominated by either the free stream component or a flapping component (that is, gliding or hovering). The kinematic assumptions, however, are easily relaxed, and the relevant normal force coefficient, C_n, can be computed by rearranging equations given above. Such an exercise would prove fruitless for the stickleback stroke since C_n must change radically along the fin's span, at least during the recovery stroke and the stroke transitions.

Given the detailed kinematics of a fin or wing, however, it is possible to drop the equal coefficient assumption as well and collapse the problem of finding the normal force at the

spanwise center of force. The total force on a fin at any point in the stroke cycle is:

$$F_{\text{measured(t)}} = [L'^2_{(t)} + T'^2_{(t)}]^{\frac{1}{2}} , \quad (25)$$

where $$L'_{(t)} = L_{\text{measured(t)}}/\{2[\sin\gamma_{(t)} \cos^2\theta_f + \sin^2\theta_f]\} , \quad (26)$$

$$T'_{(t)} = T_{\text{measured(t)}}/\{2[\sin\gamma_{(t)} \sin^2\theta_f + \cos^2\theta_f]\} . \quad (27)$$

The normal force coefficient on an airfoil is $k_{(t)} \sin\alpha'_{(r,t)}$, hence:

$$F_{N(t)} = \frac{\rho\Delta r}{2} k_{(t)} \Sigma c_{(r,t)} v^2_{(r,t)} \sin\alpha'_{(r,t)} , \quad (28)$$

where $k_{(t)}$ is an unknown proportionality factor that is constant along the span but varies over time. Substituting $F_{\text{measured(t)}}$ for $F_{N(t)}$ and rearranging, this proportionality factor becomes:

$$k = 2F_{\text{measured(t)}} \Big/ \left(\frac{\rho\Delta r}{2} \Sigma c_{(r,t)} v^2_{(r,t)} \sin\alpha'_{(r,t)} \right) . \quad (29)$$

The spanwise center of force (or mean moment) is:

$$r_{F(t)} = (\rho\Delta r/2) k_{(t)} \Sigma[r c_{(r,t)} v^2_{(r,t)} \sin\alpha'_{(r,t)}]/F_{\text{measured(t)}} . \quad (30)$$

Using the standardized center of force, $\hat{r}_{F(t)}=r_{F(t)}/R$, the 'measured' power, summed over both fins, is:

$$P_{\text{measured(t)}} = F_{\text{measured(t)}}\{\dot{h}_{(r,t)} \cos[\hat{r}_{F(t)} \alpha_{(R,t)} + \delta\sin\gamma_{(t)}] + [\hat{x}_o - \hat{x}_{r(r)}] c_{(r,t)} \hat{r}_F \dot{\alpha}_{(R,t)}\} . \quad (31)$$

The 'measured' mechanical efficiency is:

$$\eta_{\text{measured}} = \frac{\bar{T}_{\text{measured}} U}{\bar{P}_{\text{measured}}} , \quad (32)$$

where the means are taken over the stroke cycle.

Standardization

Measured and modeled forces are compared among sequences by standardizing using:

$$C_{F(t)} = \frac{F_{(t)}}{\rho A (2 r_2 n \Phi)^2} , \quad (33)$$

where A is the summed area of both pectoral fins, and r_2 is the radial second moment of area.

Results

Morphometrics

The pectoral fin of the *Gasterosteus aculeatus* articulates with the body at a relatively steep angle ($\bar{\theta}_b$=69.0±3.0°), has a modest aspect ratio for fish (AR=3.0±0.2) and high size-standardized radial moments of area ($\bar{\hat{r}}_1$=0.61±0.02, $\bar{\hat{r}}_2$=0.66±0.02, $\bar{\hat{r}}_3$=0.69±0.02) (Table 1).

Kinematics

The stroke of the threespine stickleback is qualitatively described and illustrated above (see Materials and methods/ Kinematics). Additionally, animated GIF and QuickTime® videos of selected sequences are available at http://www.usm.maine.edu/~walker/movies.html. As speed increases from 1.4 L s^{-1} to 2.8 L s^{-1}, the stroke plane angle from the vertical (β), which is numerically equivalent to the flapping angle (θ_f), decreases from 61.3° to 54.5° (P=0.04), the stroke angle increases from 94.7° to 104° (P=0.04), and the frequency increases from 4.3 Hz to 4.8 Hz (P=0.05) (Table 2). These kinematic changes are modest, which should not be surprising given that the top speed measured in this study is about half the pectoral fin powered critical swimming speed measured for this species.

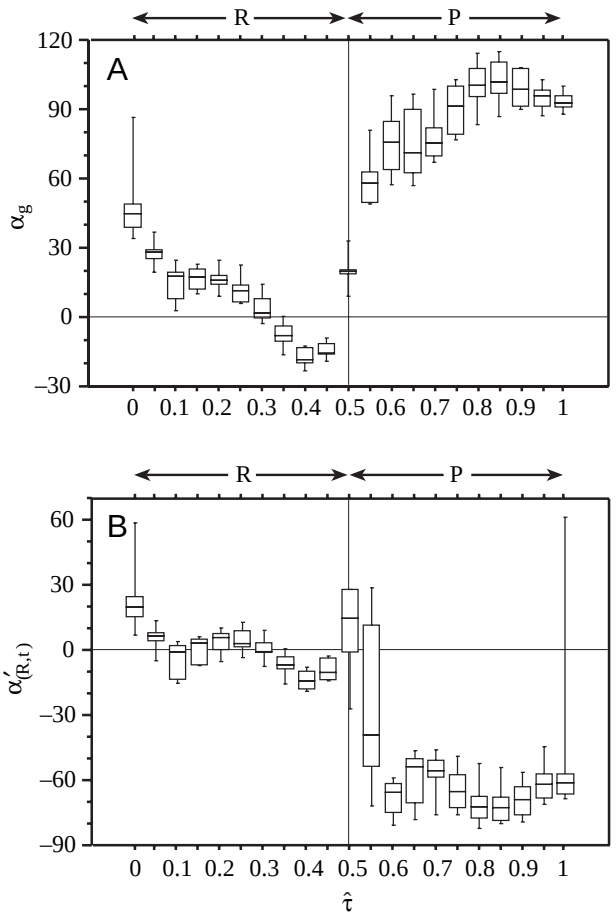

Fig. 2. Angles of attack for the distal fin chord. The time axis has been standardized within the recovery (R) and power (P) strokes. The boxplot represents the 10th (lower bar), 25th (lower edge of box), 50th (bar in box), 75th (upper edge of box) and 90th (upper bar) percentiles. (A) Geometric angle of attack, which shows a relatively feathered distal chord during the recovery stroke and broadside distal chord during the power stroke. (B) Hydrodynamic angle of attack (angle of incidence) showing the very small angles during the recovery stroke and very large angles during the power stroke.

The geometric angle of attack, α_g, at the distal chord decreases rapidly from 90° to ~15° during the first part of the recovery stroke, decreases to about –15° near the end of the recovery stroke, and rapidly rises to near 90° during the power stroke (Fig. 2). The values above 90° at the end of the power stroke indicate that the distal chord is positively twisted (positive α).

Table 1. *Body and fin morphometry for six stickleback (*Ga*1–*Ga*6) in this study*

	*Ga*1	*Ga*2	*Ga*3	*Ga*4	*Ga*5	*Ga*6	Mean±S.E.M.
L (cm)	6.64	6.80	7.68	7.31	7.11	7.22	7.13±0.37
M (g)	4.28	3.68	4.69	4.18	4.10	3.44	4.06±0.44
θ_b (deg.)	68.0	73.3	72.2	66.8	66.7	67.0	69.0±3.0
AR	3.0	2.8	2.7	3.0	3.2	3.2	3.0±0.2
$\hat{r}_1$	0.61	0.60	0.62	0.61	0.58	0.62	0.61±0.02
$\hat{r}_2$	0.67	0.65	0.67	0.66	0.62	0.67	0.66±0.02
$\hat{r}_3$	0.70	0.68	0.71	0.69	0.65	0.70	0.69±0.02

L, length; M, mass; θ_b, angle of fin base relative to horizontal; AR, aspect ratio; $\hat{r}$, non-dimensional radial position along fin span.

The angle of incidence, $\alpha'_{(R,t)}$, at the distal chord rapidly decreases to a plateau of about 5° during the first part of the recovery stroke (Fig. 2). The transition from the recovery to the power stroke is characterized by the $\alpha'_{(R,t)}$ at the distal segment decreasing to about –10° near the end of the recovery stroke, rapidly increasing to about +10° at maximum abduction and rapidly decreasing to about –80° at the beginning of the power stroke. Note that $\alpha'_{(R,t)}$ in Fig. 2 slightly differs from previously published estimates from the same data (Walker and Westneat, 2002a) because the previous data were based on normal and chordwise flow estimates (equations 8, 9 above) that failed to include the generalization for the angled fin base [$\delta\sin\gamma_{(t)}$].

Inspection of the accelerations for the three sequences digitized three times each indicates the robustness of the acceleration estimates (Fig. 3). Acceleration estimates were converted to measured force coefficients for 18 sequences at three different speeds (12.6 cm s^{-1}, 18 cm s^{-1} and 23.4 cm s^{-1}). These speeds will be referred to as low, medium and high, respectively. Each C_T and C_L curve was interpolated to 21 points at 0.05$\hat{\tau}$ increments using a cubic spline. Using these binned values, $\bar{\bar{C}}_F$ is the grand mean C_T or C_L, averaged over all sequences, for any single time increment, while $\bar{C}_F$ is the group mean C_T or C_L, averaged over all sequences within one speed class, for any single time increment (where the group is low, medium or high speed).

Force coefficients are illustrated in Fig. 4. Measured thrust coefficients, C_T, are negative and small (peak $\bar{\bar{C}}_T$=–0.25) throughout the recovery stroke. Immediately following the stroke transition, C_T rises to large, positive values (peak $\bar{\bar{C}}_T$=1.25). The peak $\bar{C}_T$ at high speeds is significantly greater than the peaks at low and medium speeds (Tukey HSD, P<0.05). The power stroke peak $\bar{\bar{C}}_T$ occurs at 0.75$\hat{\tau}$. While peak $\bar{C}_T$ occurs at 0.75$\hat{\tau}$ at the two lower speeds, it occurs at 0.65$\hat{\tau}$ at high speeds. Measured C_L gradually rises to moderately positive values (peak $\bar{\bar{C}}_L$=–0.59) during the recovery stroke and falls to very small negative values (peak $\bar{\bar{C}}_L$=–0.09) during the power stroke. There is no difference in

Table 2. *Kinematics of pectoral fin rowing at two relative swimming speeds*

	N	1.4 L s^{-1}	2.8 L s^{-1}	P
β (deg.)	20	61.3	54.5	0.0374
Φ (deg.)	20	94.7	104	0.04
n	18	4.3	4.8	0.053
k	18	0.73	0.43	0.003

β, stroke plane angle; Φ, stroke angle; n, stroke frequency; N, number of fish; k, proportionality coefficient.

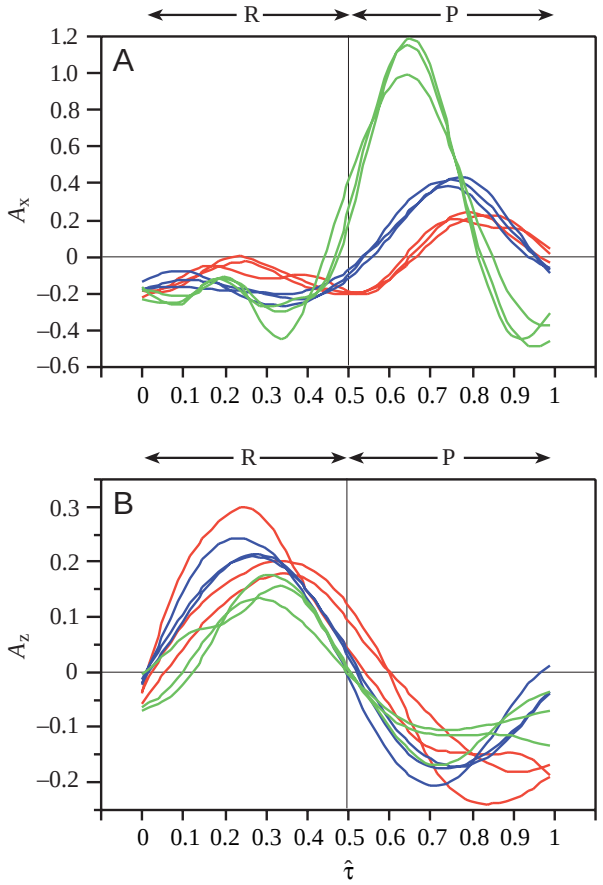

Fig. 3. Repeated measurements of body acceleration in (A) fore–aft and (B) up–down directions. The green, blue and red colors represent three different sequences while the replication within each color represents three different digitizations of the same sequence using different marks on the fish body (each located near the center of mass). The time axis has been standardized within the recovery (R) and power (P) strokes.

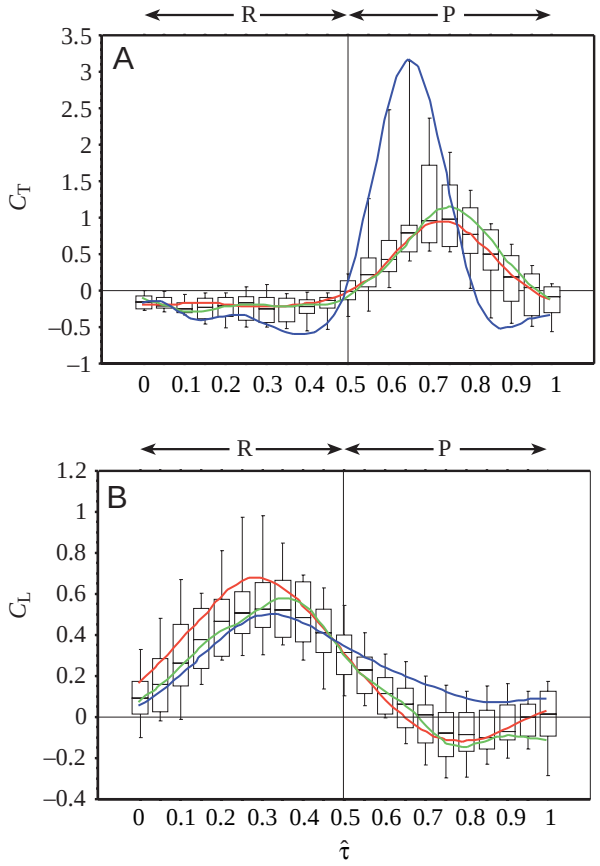

Fig. 4. Distribution of coefficients of measured thrust (C_T) and lift (C_L) throughout the standardized stroke cycle. The time axis has been standardized within the recovery (R) and power (P) strokes. The red, green and blue lines are cubic splines fit to the data at 12.6, 18.0 and 23.4 cm s^{-1}, respectively. Peak C_T does not differ between speeds. Peak C_L for the 12.6 cm s^{-1} group is significantly greater than the peak C_L for the 18.0 and 23.4 cm s^{-1} groups. Interpretation of the boxplot as in Fig. 2.

peak $\bar{C}_L$ between speeds during the recovery stroke, but the minimum $\bar{C}_L$ during the power stroke of the high speeds is more positive than those for the low and middle speeds (Tukey HSD, $P<0.05$). The recovery stroke peak $\bar{\bar{C}}_L$ occurs at $0.3\hat{\tau}$ while the power stroke minimum $\bar{\bar{C}}_L$ occurs at $0.8\hat{\tau}$. The recovery stroke peak $\bar{C}_L$ occurs at $0.3\hat{\tau}$ for both the low and high speeds but at $0.35\hat{\tau}$ for the middle speeds. The power stroke minimum $\bar{C}_L$ occurs at $0.8\hat{\tau}$ for both low and middle speeds and at $0.85\hat{\tau}$ for the high speeds.

The quasi-steady model was applied to six sequences, three each at speeds of 12.6 cm s^{-1} and 18 cm s^{-1} (Fig. 5). Both the modeled and measured C_T and C_L curves for the six sequences were interpolated to 21 points at $0.05\hat{\tau}$ increments using a cubic spline. Mean coefficients for each time increment were computed for the measured and modeled coefficients. Values for the two speeds were pooled. Note that the measured mean coefficients differ from the grand mean coefficients above because they include the values of only the six sequences that were modeled.

The peak negative $\bar{C}_{T,modeled}$ during the recovery stroke is significantly more negative than the peak negative $\bar{C}_{T,measured}$ (*t*-test, $P=0.05$). Similarly, the peak $\bar{C}_{T,modeled}$ during the power stroke is significantly greater than the peak $\bar{C}_{T,measured}$ (*t*-test, $P=0.002$). The modeled thrust during the recovery stroke is dominated by the circulatory component (Fig. 5). During the power stroke, the broad modeled thrust peak is due to a large, positive added mass component that peaks at $0.65\hat{\tau}$ and a large, circulatory component that peaks at $0.75\hat{\tau}$ (Fig. 5). Both the average and the peak circulatory thrust are larger than the average and peak added mass thrust (Table 3). The timing of

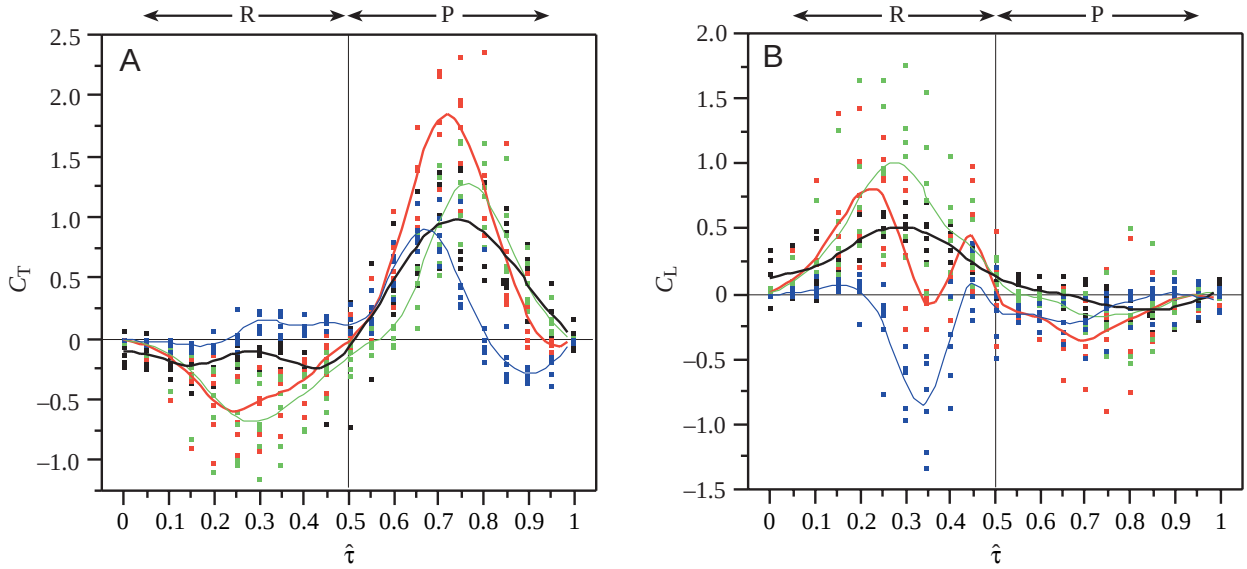

Fig. 5. Comparison of measured (black) and modeled (colored) coefficients of thrust (C_T) and lift (C_L) throughout a standardized stroke cycle. The time axis has been standardized within the recovery (R) and power (P) strokes. The red, green and blue lines are cubic splines of the total, circulatory and inertial forces, respectively, fit to the six different sequences (individual dots).

Table 3. *Measured, modeled and decomposed coefficients of thrust and lift averaged over the stroke cycle*

	C_T		C_L	
Model	Recovery	Power	Recovery	Power
Measured	–0.16	0.51	0.34	–0.01
Model	–0.30	0.72	0.34	–0.14
Circulatory	–0.35	0.48	0.51	–0.05
Added mass	0.05	0.23	–0.18	–0.09

measured peak thrust during the power stroke does not differ from the timing of the modeled and circulatory peak thrust but is significantly later than the timing of the added mass peak thrust (Table 3).

While the peak $\bar{C}_{L,modeled}$ does not differ from $\bar{C}_{L,measured}$ (P=0.07), the modeled lift curve presents two recovery stroke peaks, in contrast to the measured lift curve, which presents a single peak (Fig. 5). The two peaks in the modeled curve result from the interaction between the single, positive peak of the circulatory lift curve and the single, negative peak of the added mass lift curve (Fig. 5). The timing of the measured peak lift during the recovery stroke does not differ from the timing of the modeled, circulatory or added mass peak lift (Table 3), although the mean timing of the peak lift for the added mass model reflects the maximum positive lift occurring either much earlier (two sequences) or later (four sequences) than the measured peak (Fig. 5).

The input power estimated from the quasi-steady and measured force models have similar shapes but the quasi-steady model produces power maxima that are over twice those of the measured force model (Fig. 6). Mechanical efficiency estimated from the quasi-steady model ($\eta_{modeled}$) ranges from 0.10 to 0.22, while that estimated by the measured force model ($\eta_{measured}$) ranges from 0.13 to 0.29 (Table 4).

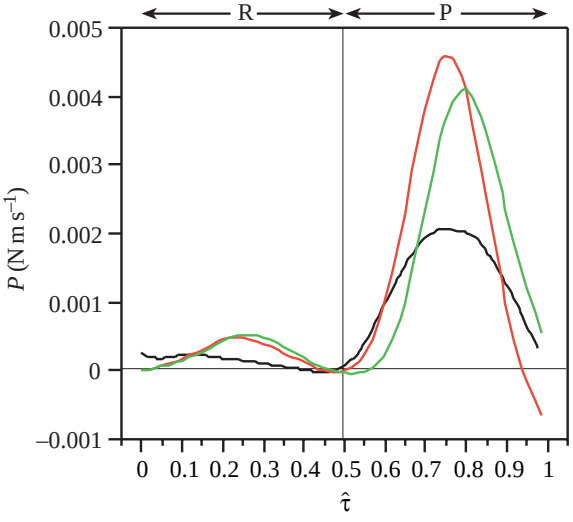

Fig. 6. Measured (black) and modeled total (red) and circulatory (green) power required to oscillate the fins. The time axis has been standardized within the recovery (R) and power (P) strokes.

Table 4. *Measured and modeled efficiencies (η) for the six measured sequences compared to the expected efficiencies (at the same reduced frequency,* k*) for the spanwise twisting and the root-rotating fins modeled in Walker and Westneat (2000)*

Sequence	k	$\eta_{measured}$	$\eta_{modeled}$	η_{exp} (twist)	η_{exp} (RR)
1	0.88	0.16	0.20	0.08	0.19
2	0.65	0.13	0.16	0.09	0.24
3	0.71	0.13	0.13	0.09	0.23
4	0.74	0.27	0.15	0.09	0.22
5	0.58	0.29	0.22	0.09	0.27
6	0.47	0.24	0.10	0.07	0.33
Mean	0.67	0.20	0.16	0.09	0.25

Discussion

Notes on the method for estimating the force balance

Lift and thrust balances were estimated for free-swimming sticklebacks. The accuracy of these estimates is a function of the accuracy of several components: measured body accelerations in the anterior-posterior and dorso-ventral directions, measured body mass, measured weight in water, modeled added mass and modeled parasite drag. Measured acceleration error affects both the magnitude of the lift and thrust and the shape of the lift and thrust curves. The error in the measured mass and added mass of the fish affects the scale of the curve but not its shape. The error in estimating the parasite drag and the weight (in water) of the fish affects only the position of the curve along the y-axis. The error due to estimating the mass of the fish is trivial, while the error in the estimation of the added mass is unknown. The errors in estimating the weight in water and the parasite drag are unknown but the fact that the thrust and lift coefficients are near zero when the fin is against the body suggests that any error in the estimate of weight and drag is small.

By far the largest error component is that due to estimating accelerations, and this error can influence both the shape of the curve and the magnitude of the peaks. The error in the acceleration estimates has two sources: precision, or the ability to repeatedly measure the same value, and accuracy, or the ability to measure the true value. The precision of the acceleration estimates can be estimated using the three sequences that were measured three times each. Within any sequence, there are three estimates of the maximum forward acceleration during the power stroke and the maximum upward acceleration during the recovery stroke. The percent deviation of any one estimate from the mean of the three estimates is $|A_{max}–\bar{A}_{max}|/\bar{A}_{max}\times100$. The maximum percent deviations for the maximum forward acceleration were 6%, 9% and 11% for the three different sequences. The maximum percent deviations for the maximum upward acceleration were 9%, 14% and 33% for the three different sequences.

Precise estimates suggest accurate estimates, but this may not be the case if there is some unknown factor that consistently biases the numerical differentiation method. The MSE quintic spline algorithm has a consistent downward bias

in the estimate of maximum accelerations (Walker, 1998). This bias could be corrected if there were a known relationship between bias and some measurable parameter summarizing the data. One potential parameter is the relative noise, ν (or roughness parameter), in the data (Corradini et al., 1993):

$$\nu = \frac{\sigma_{noise}}{\sigma_{signal}} \times 100 \quad (34)$$

where σ_{signal} is the standard deviation of the smoothed displacement (after removing any net translation over the stroke cycle) and σ_{noise} is the standard deviation of the difference between the raw and smoothed values (again, after removing the net translation). The ν for the six, modeled sequences ranged from 18% to 36% in the *x*-direction and from 58% to 122% in the *z*-direction. Unfortunately, the relationship between ε and ν at these levels of error has not been explored but an extrapolation of the data from Walker (1998) suggests that the bias for the MSE quintic spline algorithm in this range of ν lies between –25% and –50%.

Clearly, there is a great need for further exploration in this area if we are going to advance our knowledge of locomotor control from studies of freely moving animals. Nevertheless, the reasonable consistency between repeated estimates of accelerations from the same sequence, between estimates of accelerations among sequences and between accelerations and the quasi-steady model suggests the method should be exploited more often.

Dynamics of pectoral fin rowing

Recent work on robotic insect wings has elegantly shown the importance of an attached vortex augmenting the circulatory force during the translational and, in *Drosophila*, the rotational phases of the stroke cycle (pronation and supination in *Drosophila* are confined to short intervals bounding the stroke transitions; Ellington et al., 1996; Dickinson et al., 1999). The absence of a peak in the measured force curves (Fig. 4) near the transition from recovery to power stroke suggests that circulatory forces at this point in the stroke cycle are trivial. This result may seem surprising given the rapid change in the angle of attack during this part of the stroke (Fig. 2). Again, as described in the Materials and methods, this change in attack angle is only occurring at the extreme leading edge region of the fin (a relatively small area). Following this rotation of the leading edge, the subsequent rays are simply translated posteriorly.

The quasi-steady circulatory forces based on the unsteady coefficients are significantly greater than the measured forces. The power stroke force maxima is generated by a fin that is translating with the distal half at an attack angle, α', of ~70° (Fig. 2). The equilibrium drag coefficient for a flat plate at 70° to the flow at the *Re* relevant to stickleback swimming is 1.1 (Hoerner, 1965) while the corresponding unsteady coefficient is 3.0. The high maximum $\bar{C}_{T,circulatory}$, relative to $\bar{C}_{T,measured}$, raises the possibility that the unsteady coefficients are too high to accurately model the dynamic environment of the stickleback fin, perhaps because the unsteady coefficients were measured at a smaller *Re*. The range of noise–signal ratios, ν, discussed above suggests that, alternatively, the measured force estimates are too low because the quintic spline algorithm has a consistent downward bias in the estimation of maximum second derivatives (Walker, 1998).

At the *Re* of pectoral fin rowing in the stickleback, the acceleration reaction should have a large influence on the force balance. To optimize the acceleration reaction, the fin should oscillate along a horizontal stroke plane with the fin surface oriented normal to its motion along its entire span throughout the stroke. For the six digitized fin sequences, the acceleration reaction component of the thrust balance would have an optimal peak $C_{T,AddedMass}$ of about 1.8 occurring at the stroke transition ($0.5\hat{\tau}$) (Fig. 6). By contrast, $\bar{C}_{T,measured}$ at $0.5\hat{\tau}$ does not differ from 0, which suggests that the stickleback's fin motion is not optimizing the acceleration reaction. Indeed, the estimated acceleration reaction curve has a much smaller ($C_{T,AddedMass}$=0.88) and later ($0.65\hat{\tau}$) peak (Fig. 6). Instead of dominating the force balance, the acceleration reaction contributes about half as much to the thrust balance as the circulatory force (Table 3). The estimated acceleration reaction at $0.5\hat{\tau}$ is much smaller than the optimal acceleration reaction at $0.5\hat{\tau}$ because the fin is beautifully feathered at this point in the stroke cycle and simply cannot accelerate a large volume of fluid with this orientation. While the modeled acceleration reaction is significantly less than the modeled circulatory force, the shape of the C_T and, especially, C_L curves suggests that the influence of the acceleration reaction may be even less than indicated by the model.

The acceleration reaction model presented for the stickleback differs radically from that presented for the angelfish, *Pteryphylum emekei* (Blake, 1979). Blake (1979) argued that the positive contribution to the thrust balance at the beginning of the power stroke canceled the negative contribution to the thrust balance at the end of the power stroke with the net result of zero contribution of the acceleration reaction to the thrust balance. Given the kinematics used by Blake (1979), in which the fin was apparently oriented broadside to its motion throughout the entire power stroke, the acceleration reaction during the power stroke should have resembled the second half of the optimal acceleration reaction curve in Fig. 6.

Reduced recovery stroke drag

A major influence on the mechanical efficiency of the rowing fin is the recovery stroke geometry (Walker and Westneat, 2000; Walker, 2002a). For efficient rowing, the recovery stroke should generate little drag or lift. Reduced loading can be achieved by minimizing fin speed, fin area or fin angle of attack. Animals with jointed limbs typically minimize average limb speed by flexing the limbs (actively or passively) during the recovery stroke (Walker, 2002a; this works because speed is a function of both angular velocity and radial distance from the limb base). Limb area is reduced in some animals by collapsing webbed limbs or swimming hairs (Hughes, 1958; Nachtigall, 1974; Koehl, 1993). Limb angle of

attack is reduced in larger animals by feathering the appendage (Walker, 2002a).

Stickleback fins are supported by bony fin rays that lack movable joints, except at the fin base, and the rays are too stiff to allow the passive flexion necessary for substantial speed reduction. While adducting the fin rays can reduce fin area, sticklebacks do not exploit this mechanism to reduce loading during the recovery stroke. The primary kinematic mechanism used by sticklebacks to reduce loading during the recovery stroke is angle of attack reduction by fin feathering. Feathering requires the stickleback to twist its fin down its span. While the kinematic model used to estimate forces on the recovery stroke assumed that the fin twisted linearly along the span, the much smaller measured drag relative to modeled drag suggests that the stickleback is able to feather its fin more effectively than expected by the model.

Feathering the appendage presents a second obstacle to efficient swimming because the fin must be rotated into the feathered orientation. Any form of stiff rotation would generate substantial drag. As an alternative, the stickleback peels its fin off its body. By rotating the trailing portion of the fin dorsally along the body while the leading region peels off in a feathered orientation, the fin generates little drag.

The final obstacle presented by a feathered appendage is the optimal rotation back into a broadside orientation to start the power stroke. Instead of stiffly rotating into a broadside orientation, a wave of re-orientation passes from leading edge to trailing edge. This kinematic mechanism results in a resultant force that is largely confined to the frontal plane, producing thrust and lateral forces with very little lift. By contrast, a rapid, stiff rotation about a spanwise axis lying posterior to the chordwise center of pressure would generate thrust and a large, negative lift.

While the net drag during the recovery stroke is small, substantial lift is generated. This lift balances the weight of the fish but it is unclear if the stickleback maintains negative buoyancy to balance the lift necessarily generated by a fin that cannot feather more optimally (because of the higher α_m toward the fin base) or if the fin is generating lift in order to balance an obligately negatively buoyant body.

Energetics

The mean $\eta_{modeled}$ (0.16) and $\eta_{measured}$ (0.2) lie in between the mean optimal η of twisted (0.08) and perfectly feathered (0.24) rowing fins oscillating at equivalent reduced frequencies. Stickleback rowing efficiency is expected to be better than that of the model twisted fin for several reasons. First, the stickleback fins expand distally, a shape that has been shown to optimize rowing performance (Blake, 1981). Second, the stickleback fin articulates with the body at an angle of 69° compared with an angle of 90° for the model fin. The average angle of attack along the span in the stickleback fin should be less than that for the model twisted fin. Finally, the dynamic data discussed above, and possibly these energetic data, suggest that the stickleback may be able to feather its fin along its span better than expected by a linearly twisted model.

The mean efficiency estimated by the quasi-steady blade-element model is exactly that estimated by a quasi-steady model for the rowing fin of the angelfish (Blake, 1979, 1980). As the models differ in the geometry of the angle of attack, the source of the empirical force coefficients and, importantly, the model of drag on the fins (Walker and Westneat, 2000), this similarity is partly coincidence. Blake (1979) used a dead-drag measure of a fish with its pectoral fins extended out from its body as the measure of parasite drag. But the parasite drag that a rowing fish has to work against does not include the pressure drag produced by extended pectoral fins because these have a time-averaged pressure distribution that results in net thrust, not drag on the ‘vehicle’. Consequently, the fins only need to work against the parasite drag of the body and any viscous drag on the pectoral fins (the viscous drag on the pectoral fins was not included in the model of mechanical efficiency because of the difficulty of estimating this parameter for a deforming, oscillating body). A similar argument was made for fishes that power swimming by body and caudal fin undulations, although these authors argue that the body does not even work against its own viscous drag and, consequently, the concept of efficiency (for a self-propelled, undulating fish) is meaningless (Schultz and Webb, 2002).

The measured efficiencies in this study are supported by the only other comparable data collected by an independent method: an optimal efficiency of 0.15 measured from the motor-controlled rowing stroke of a stiff fin modeled on the pectoral fin of the largemouth bass, *Micropterus salmoides* (Kato, 1999). Combined, the quasi-steady model, the measured-force model and the motor-driven physical model all indicate that rowing is a relatively inefficient means of transport, at least relative to a flapping-fin mechanism (Walker and Westneat, 2000).

This conclusion, that rowing is an inefficient propulsive mechanism, raises an interesting paradox. Marine sticklebacks are anadromous fishes, migrating hundreds of kilometers between the open ocean and spawning sites in either estuaries or freshwater streams (Wootton, 1976; Cowen et al., 1991). Marine sticklebacks power these steady cruising behaviors using only pectoral fin rowing. Indeed, they lack the band of slow, oxidative (red) muscle fibers in their axial musculature (te Kronnie et al., 1983) that is necessary for powering steady, BCF locomotion (Jayne and Lauder, 1994).

Why don’t sticklebacks have the high aspect ratio, tapered, flapping pectoral fins common to fishes that swim with greater endurance (Walker and Westneat, 2000, 2002a; Bellwood and Wainwright, 2001; Fulton et al., 2001)? The design of the stickleback shoulder and fin could reflect a trade-off between optimal designs for continuous swimming and other behaviors such as low-speed maneuvering or nest fanning. Alternatively, rowing could reflect an ontogenetic constraint due to the low *Re* experienced by the fins of juvenile sticklebacks. Anadromous juvenile sticklebacks have been found hundreds of kilometers offshore, and available data indicate that these juveniles have the endurance to actively swim long distances (Stevens, 1993). The mean *Re* for a 20 mm stickleback swimming from 1 *BL* s^{-1} to

3 *BL* s^{-1} is approximately 50 to 60. Available published data suggest that no aquatic animals swim by flapping appendages below *Re*≈80–100 (Walker, 2002a), which supports the hypothesis that juvenile sticklebacks must row to swim effectively. While viscous forces on a fin are strongly influencing fin performance at *Re*<100, a simulated comparison of rowing and flapping fins showed that rowing is not expected to outperform flapping until an *Re* less than ~20 is reached (Walker, 2002a). Furthermore, rowing fins at these low *Re* (<50) must use a combination of reduced fin area and recovery stroke speed (see above) in order to outperform flapping because feathering is not an effective mechanism in this *Re* range (Walker, 2002a). If juveniles have the same recovery stroke kinematics as found in adults, the efficiency of the juvenile fin stroke should be much lower than if it were oscillating with a flapping geometry. This suggests that active swimming at *Re*<100 is not a constraint on the design of the stickleback fin.

Conclusions

The threespine stickleback swims at sub-burst speeds by generating thrust from paired pectoral fins that present a stereotypical rowing stroke. While the rowing stroke is inefficient relative to a flapping stroke (Walker and Westneat, 2000), the design of the stickleback fin, with its multiple, independently actuated bony struts supporting a thin, flexible membrane, results in less wasted energy than would occur if the fin were rowing as a stiff, flat plate. This design feature, which is common to actinopterygian fishes (Lauder and Drucker, in press; Westneat et al., in press), presents a difficult challenge for constructing detailed models of pectoral fin function (specifically) or the performance consequences of pectoral fin design variation (more generally). Addressing either this specific or more general question will require a joint research effort combining the state-of-the-art computational, visual and physical modeling tools (Gharib et al., 2002; Lauder and Drucker, in press; Mittal, in press; Triantafyllou et al., in press) with the more traditional methods exploited here.

List of symbols

A	total pectoral fin area
A_{wet}	wetted area of fish body
b_{max}	maximum body breadth
$\bar{c}$	mean chord
$c_{(r)}$	chord length
$\bar{C}_F$	group mean force
$\bar{\bar{C}}_F$	grand mean force
C_D	parasite drag coefficient on body
$C'_{D(r,t)}$	sectional drag coefficient
C_L	mean lift coefficient
$C'_{L(r,t)}$	sectional lift coefficient
C_T	mean thrust coefficient
D	parasite drag of body
$dD_{a(r,t)}$	aft component of added mass force
$dD_{c(r,t)}$	aft component of circulatory force
$dD'_{(r,t)}$	circulatory drag
$dF_{a(r,t)}$	added mass force
$dF_{n(r,t)}$	normal component of circulatory force
$dF_{x(r,t)}$	chordwise component of circulatory force
$dL_{a(r,t)}$	upward component of added mass force
$dL_{c(r,t)}$	upward component of circulatory force
$dL'_{(r,t)}$	circulatory lift
d_{max}	maximum body depth
$dP_{a(r,t)}$	sectional inertial power
$dP_{c(r,t)}$	sectional circulatory power
$dT_{a(r,t)}$	added mass thrust
$dT_{c(r,t)}$	circulatory thrust
f	fineness ratio
$F_{measured}$	measured force on fin
$F_{N(t)}$	normal force on fin
F_x	fore–aft component of measured force on body
F_z	dorso-ventral component of measured force on body
$h_{(r,t)}$	heaving velocity
$k_{(t)}$	proportionality coefficient
l	standard length of fish body
$L_{measured(t)}$	indirectly measured lift on body
$L_{modeled(t)}$	modeled lift on body
M_A	fish added mass
M_F	fish mass
n	stroke frequency
$P_{modeled(t)}$	modeled power on body
R	fin length
$\hat{r}$	non-dimensional radial position along fin span
r	radial position along fin span
r_2	radial second moment of area
Re	Reynold's number
$r_{F(t)}$	radial center of force along fin span
T	period of stroke cycle
t	time in stroke cycle
$T_{measured(t)}$	indirectly measured thrust on body
$T_{modeled(t)}$	modeled thrust on body
U	free stream speed of flow
$U_{n(t)}$	normal component of free stream
$v_{(r,t)}$	velocity of fin element
$v_{n(r,t)}$	normal velocity of fin element
$v_{x(r,t)}$	chordwise velocity of fin element
W	weight of body in water
$\hat{x}_i$	non-dimensional chordwise location of center of incident flow
$\hat{x}_{r(r)}$	non-dimensional chordwise location of center of rotation
Δr	width of fin blade element
Φ	stroke angle
$\alpha_{(r,t)}$	fin pitch
$\alpha_{g(t)}$	geometric angle of attack
α_R	pitch of the functional portion of the fin
$\alpha'_{(r,t)}$	angle of incidence
β	stroke plane angle (relative to vertical)
$\gamma_{(t)}$	azimuthal position of fin
δ	angle between fin base and flapping axis
η	mechanical efficiency

μ	added mass coefficient
θ_b	angle of fin base relative to horizontal
θ_f	flapping axis (normal to stroke plane)
ρ	water density
τ	stroke period
$\hat{\tau}$	standardized stroke period

Ideas presented here greatly benefited from spirited discussions with Tom Daniel, Michael Dickinson, Frank Fish, George Lauder, Paul Webb, Mark Westneat and Brad Wright. Two anonymous reviewers are gratefully acknowledged for improving the manuscript. This work was supported by a National Science Foundation Postdoctoral Fellowship in the Biosciences Related to the Environment, Office of Naval Research N00014-01-1-0506, Office of Naval Research grant N00014-99-0184 to M. Westneat and J. Walker, and the Bioscience Research Institute of Southern Maine.

References

Anderson, E. J., McGillis, W. R. and Grosenbaugh, M. A. (2001). The boundary layer of swimming fish. *J. Exp. Biol.* **204**, 81-102.

Archer, S. D. and Johnston, I. A. (1989). Kinematics of labriform and subcarangiform swimming in the Antarctic fish *Notothenia neglecta*. *J. Exp. Biol.* **143**, 195-210.

Arreolla, V. I. and Westneat, M. W. (1996). Mechanics of propulsion by multiple fins: kinematics of aquatic locomotion in the burrfish (*Chilomycterus schoepfi*). *Proc. R. Soc. Lond. B.* **263**, 1689-1696.

Bell, M. A. and Foster, S. A. (1994). *The Evolutionary Biology of the Threespine Stickleback.* Oxford: Oxford University Press.

Bellwood, D. R. and Wainwright, P. C. (2001). Locomotion in labrid fishes: implications for habitat use and cross-shelf biogeography on the Great Barrier Reef. *Coral Reefs* **20**, 139-150.

Blake, R. W. (1979). The mechanics of labriform locomotion. I. Labriform locomotion in the angelfish (*Pterophyllum eimekei*): an analysis of the power stroke. *J. Exp. Biol.* **82**, 255-271.

Blake, R. W. (1980). The mechanics of labriform locomotion II. An analysis of the recovery stroke and the overall fin-beat cycle propulsive efficiency in the angelfish. *J. Exp. Biol.* **85**, 337-342.

Blake, R. W. (1981). Influence of pectoral fin shape on thrust and drag in labriform locomotion. *J. Zool. Lond.* **194**, 53-66.

Breder, C. M., Jr (1926). The locomotion of fishes. *Zoologica* **4**, 159-291.

Brennen, C. E. (1982). A review of added mass and fluid inertial forces. *Report No. CR82.010.* Port Hueneme, CA: Naval Civil Engineering Laboratory.

Corradini, M. L., Fioretti, S. and Leo, T. (1993). Numerical differentiation in movement analysis: how to standardise the evaluation of techniques. *Med. Biol. Eng. Comput.* **31**, 187-197.

Cowen, R. K., Chiarella, L. A., Gomez, C. J. and Bell, M. A. (1991). Offshore distribution, size, age, and lateral plate variation of late larval/early juvenile sticklebacks (*Gasterosteus*) off the Atlantic coast of New Jersey and New York. *Can. J. Fish. Aquat. Sci.* **48**, 1679-1684.

DeLaurier, J. D. (1993). An aerodynamic model for flapping-wing flight. *Aeronaut. J.* **97**, 125-130.

Dickinson, M. H., Lehmann, F.-O. and Sane, S. P. (1999). Wing rotation and the aerodynamic basis of insect flight. *Science* **284**, 1954-1960.

Drucker, E. G. and Jensen, J. S. (1997). Kinematic and electromyographic analysis of steady pectoral fin swimming in the surfperches. *J. Exp. Biol.* **200**, 1709-1723.

Drucker, E. G. and Lauder, G. V. (1999). Locomotor forces on a swimming fish: three-dimensional vortex wake dynamics quantified using digital particle image velocimetry. *J. Exp. Biol.* **202**, 2392-2412.

Drucker, E. G. and Lauder, G. V. (2000). A hydrodynamic analysis of fish swimming speed: wake structure and locomotor force in slow and fast labriform swimmers. *J. Exp. Biol.* **203**, 2379-2393.

Drucker, E. G. and Lauder, G. V. (2001). Wake dynamics and fluid forces of turning maneuvers in sunfish. *J. Exp. Biol.* **204**, 431-442.

Drucker, E. G. and Lauder, G. V. (2003). Function of pectoral fins in rainbow trout: behavioral repertoire and hydrodynamic forces. *J. Exp. Biol.* **206**, 813-826.

Ellington, C. P. (1984a). The aerodynamics of hovering insect flight. II. morphological parameters. *Phil. Trans. R. Soc. Lond. B* **305**, 17-40.

Ellington, C. P. (1984b). The aerodynamics of hovering insect flight. IV. Aerodynamic mechanisms. *Phil. Trans. R. Soc. Lond. B* **305**, 79-113.

Ellington, C. P., Van den Berg, C. and Willmott, A. P. (1996). Leading-edge vortices in insect flight. *Nature* **384**, 626-630.

Fulton, C. J., Bellwood, D. R. and Wainwright, P. C. (2001). The relationship between swimming ability and habitat use in wrasses (Labridae). *Mar. Biol.* **139**, 25-33.

Fung, Y. C. (1993). *An Introduction to the Theory of Aeroelasticity*. New York: Dover.

Geerlink, P. J. (1983). Pectoral fin kinematics of *Coris formosa* (Teleostei, Labridae). *Neth. J. Zool.* **33**, 515-531.

Gharib, M., Pereira, F., Dabiri, D., Hove, J. R. and Modarress, D. (2002). Quantitative flow visualization: toward a comprehensive flow diagnostic tool. *Integ. Comp. Biol.* **42**, 964-970.

Gibb, A., Jayne, B. C. and Lauder, G. V. (1994). Kinematics of pectoral fin locomotion in the bluegill sunfish *Lepomis macrochirus*. *J. Exp. Biol.* **189**, 133-161.

Gordon, M. S., Chin, H. G. and Vojkovich, M. (1989). Energetics of swimming in fishes using different methods of locomotion. 1. Labriform swimmers. *Fish Physiol. Biochem.* **6**, 341-352.

Gordon, M. S., Plaut, I. and Kim, D. (1996). How puffers (Telostei: Tetraodontidae) swim. *J. Fish Biol.* **49**, 319-328.

Hoerner, S. F. (1965). *Fluid-Dynamic Drag.* Midland Park, NJ: S. F. Hoerner.

Hove, J. R., O'Bryan, L. M., Gordon, M. S., Webb, P. W. and Weihs, D. (2001). Boxfishes (Teleostei: Ostraciidae) as a model system for fishes swimming with many fins: kinematics. *J. Exp. Biol.* **204**, 1459-1471.

Hughes, G. (1958). The co-ordination of insect movements. 3. Swimming in *Dytiscus*, *Hydrophilus*, and a dragonfly nymph. *J. Exp. Biol.* **35**, 567-583.

Jayne, B. C. and Lauder, G. V. (1994). How swimming fish use slow and fast muscle fibers: implications for models of vertebrate muscle recruitment. *J. Comp. Physiol. A* **175**, 123-131.

Kato, N. (1999). Hydrodynamic characteristics of mechanical pectoral fin. *J. Fluids Eng.* **121**, 605-613.

Koehl, M. A. R. (1993). Hairy little legs: feeding, smelling, and swimming at low Reynolds numbers. *Contemp. Math.* **141**, 33-47.

Korsmeyer, K. E., Steffensen, J. F. and Herskin, J. (2002). Energetics of median and paired swimming, body and caudal fin swimming, and gait transition in parrotfish (*Scarus schlegeli*) and triggerfish (*Rhinecanthus aculeatus*). *J. Exp. Biol.* **205**, 1253-1263.

Lauder, G. V. and Drucker, E. G. (in press). Morphology and experimental hydrodynamics of piscine control surfaces. *J. Ocean Eng.*

Lauder, G. V. and Jayne, B. C. (1996). Pectoral fin locomotion in fishes: testing drag-based models using three-dimensional kinematics. *Am. Zool.* **36**, 567-581.

Lindsey, C. C. (1978). Form, function, and locomotory habits in fish. In *Fish Physiology*, vol. VII (ed. W. S. Hoar and D. J. Randall), pp. 1-100. New York: Academic Press.

Mittal, R. (in press). Computational modeling in bio-hydrodynamics: trends, challenges and recent advances. *J. Ocean Eng.*

Nachtigall, W. (1974). Locomotion: mechanics and hydrodynamics of swimming in aquatic insects. In *The Physiology of Insecta*, vol. III (ed. M. Rockstein), pp. 381-432. New York: Academic Press.

Pennycuick, C. J., Hedenström, A. and Rosén, M. (2000). Horizontal flight of a swallow (*Hirundo rustica*) observed in a wind tunnel, with a new method for directly measuring mechanical power. *J. Exp. Biol.* **203**, 1755-1765.

Pereira, F. and Gharib, M. (2002). Defocusing digital particle image velocimetry and the three-dimensional characterization of two-phase flows. *Measure. Sci. Technol.* **13**, 683-694.

Ramamurti, R., Sandberg, W. C., Löhner, R., Walker, J. A. and Westneat, M. W. (2002). Fluid dynamics of flapping aquatic flight in the bird wrasse: 3-D unsteady computations with fin deformation. *J. Exp. Biol.* **205**, 2997-3008.

Sane, S. and Dickinson, M. H. (2002). The aerodynamic effects of wing rotation and a revised quasi-steady model of flapping flight. *J. Exp. Biol.* **205**, 1087-1096.

Schultz, W. W. and Webb, P. W. (2002). Power requirements of swimming: do new methods resolve old questions? *Integ. Comp. Biol.* **42**, 1018-1025.

Srygley, R. B. and Thomas, A. L. R. (2002). Unconventional lift-generating mechanisms in free-flying butterflies. *Nature* **420**, 660-664.

Stevens, J. M. (1993). Ontogeny of sustained and prolonged swimming performance in the juvenile threespine stickleback, *Gasterosteus aculeatus* L., 1758. *MSc. Thesis.* University of Rhode Island.

te Kronnie, G., Tatarczuch, L., Raamsdonk, W. v. and Kilarski, W. (1983). Muscle fibre types in the myotome of stickleback, *Gasterosteus aculeatus* L.; a histochemical, immunohistochemical and ultrastructural study. *J. Fish Biol.* **22**, 303-316.

Triantafyllou, M., Techet, A. and Hover, F. (in press). Review of experimental work in biomimetic foils. *J. Ocean Eng.*

Usherwood, J. R. and Ellington, C. P. (2002). The aerodynamics of revolving wings. II. Propeller force coefficients from mayfly to quail. *J. Exp. Biol.* **205**, 1565-1576.

Vogel, S. and LaBarbera, M. (1978). Simple flow tanks for research and teaching. *BioSci.* **28**, 638-643.

Walker, J. A. (1998). Estimating velocities and accelerations of animal locomotion: a simulation experiment comparing numerical differentiation algorithms. *J. Exp. Biol.* **201**, 981-995.

Walker, J. A. (2002a). Functional morphology and virtual models: physical constraints on the design of oscillating wings, fins, legs, and feet at intermediate Reynolds numbers. *Integ. Comp. Biol.* **42**, 232-242.

Walker, J. A. (2002b). Rotational lift: something different or more of the same? *J. Exp. Biol.* **205**, 3783-3792.

Walker, J. A. and Westneat, M. W. (1997). Labriform propulsion in fishes: kinematics of flapping aquatic flight in the bird wrasse *Gomphosus varius* (Labridae). *J. Exp. Biol.* **200**, 1549-1569.

Walker, J. A. and Westneat, M. W. (2000). Mechanical performance of aquatic rowing and flying. *Proc. R. Soc. Lond. B* **267**, 1875-1881.

Walker, J. A. and Westneat, M. W. (2002a). Kinematics, dynamics, and energetics of rowing and flapping propulsion in fishes. *Integ. Comp. Biol.* **42**, 1032-1043.

Walker, J. A. and Westneat, M. W. (2002b). Performance limits of labriform propulsion and correlates with fin shape and motion. *J. Exp. Biol.* **205**, 177-187.

Ward, S., Möller, U., Rayner, J. M. V., Jackson, D. M., Bilo, D., Nachtigall, W. and Speakman, J. R. (2001). Metabolic power, mechanical power and efficiency during wing tunnel flight by the European starling *Sturnus vulgaris*. *J. Exp. Biol.* **204**, 3311-3322.

Webb, P. W. (1973). Kinematics of pectoral fin propulsion in *Cymatogaster aggregata*. *J. Exp. Biol.* **59**, 697-710.

Webb, P. W. (1974). Efficiency of pectoral fin propulsion of *Cymatogaster aggregata*. In *Swimming and Flying in Nature*, vol. 2 (ed. T. Y. Wu, C. J. Brokaw and C. Brennen), pp. 573-584. New York: Plenum.

Webb, P. W. and Blake, R. W. (1985). Swimming. In *Functional Vertebrate Morphology* (ed. M. Hildebrand, D. M. Bramble, K. F. Liem and D. B. Wake), pp. 110-128. Cambridge: Harvard University Press.

Westneat, M. W. (1996). Functional morphology of aquatic flight in fishes: kinematics, electromyography, and mechanical modeling of labriform locomotion. *Am. Zool.* **36**, 582-598.

Westneat, M. W., Thorsen, D. H., Walker, J. A. and Hale, M. E. (in press). Structure, function and neural control of pectoral fins in fishes. *J. Ocean Eng.*

Westneat, M. W. and Walker, J. A. (1997). Motor patterns of labriform locomotion: kinematic and electromyographic analysis of pectoral fin swimming in the labrid fish *Gomphosus varius*. *J. Exp. Biol.* **200**, 1881-1893.

Woltring, H. J. (1985). On optimal smoothing and derivative estimation from noisy displacement data in biomechanics. *Hum. Movement Sci.* **4**, 229-245.

Woltring, H. J. (1986). A Fortran package for generalized, cross-validatory spline smoothing and differentiation. *Adv. Eng. Software* **8**, 104-107.

Wootton, R. J. (1976). *The Biology of the Sticklebacks.* New York: Academic Press.